Supplementary information for

Geometry symmetry-free and Higher-order Optical Bound States in the Continuum

Qingjia Zhou[1, 2], Yangyang Fu[3], Lujun Huang[4], Qiannan Wu[5], Andrey Miroshnichenko[4], Lei Gao[1, 2] and Yadong Xu[1, 2]

[1]*School of Physical Science and Technology & Collaborative Innovation Center of Suzhou Nano Science and Technology, Soochow University, Suzhou 215006, China.*
[2]*Jiangsu Key Laboratory of Thin Films, Soochow University, Suzhou 215006, China.*
[3]*College of Science, Nanjing University of Aeronautics and Astronautics, Nanjing 211106, China.*
[4]*School of Engineering and Information Technology, University of New South Wales, Canberra, ACT, 2600 Australia.*
[5]*School of Science, North University of China, Taiyuan, Shanxi, 030051, China.*

Supplementary Note 1. Eigenmode analysis of ZIM with objects

In simulation: Full-wave simulations were carried out by using software COMSOL Multiphysics to study the eigenfrequency and eigenmode profiles. In Fig. 2, the working frequency is 15 GHz , and the linewidth vanishes at $\alpha = 0$ and $\varepsilon_d = 4.82$. For eigenmode analysis, we studied a case of a ZIM background containing two same objects of $\varepsilon_d = 4.82$ instead. The infinite ZIM is replaced by a large ZIM area with $r = 10R_1$. We obtain two eigenfrequency and corresponding field pattern as shown in Fig. 3b. For the case of two cylinders with $\varepsilon_d = 4.82, R_1 = R_2 = 8\,mm$ embedded in ZIM environment, the system supports a bright mode and a dark mode (i.e., BIC mode, at about 15 GHz). The small deviation is mainly due to inaccurate data selection and accuracy of grid division in simulations. Similar procedures were applied to the case of three cylinders with $\varepsilon_d = 4.82$ and $R_1 = R_2 = R_3 = 8\,mm$ embedded in ZIM environment. Based on numerical calculations, we can easily get the eigenfrequency of each eigenmode and its corresponding field patterns, as shown in Fig. 4b.

Theoretical analysis: It is evident from Eq. (1) that the eigenfrequency of studied system also can be strictly calculated by setting the denominator term of the Eq. (1) to be zero, that is $1-i(\pi/w)\sum_{i=1}^{N} R_i J_1\left(\sqrt{\varepsilon_d}k_0 R_i\right)\Big/\sqrt{\varepsilon_d}J_0\left(\sqrt{\varepsilon_d}k_0 R_i\right) = 0$. By solving this equation with considered geometric parameters, a complex eigenfrequency $\omega = \omega_0 - i\gamma$ can be obtained analytically, and the Q factor of the corresponding eigenmode is calculated by $Q = \omega_0/2\gamma$. Based on this method, Supplementary Fig. 1a analytically shows the calculated eigenfrequency that decreases with the increase of α . In particular, at $\alpha = 0$, the eigenfrequency is 15 GHz, which is marked with black star in plot.

In Supplementary Fig. 1b, the Q factor turns to infinite at $\alpha = 0$, where means such mode is BIC mode. These analytical results are consistent with those based on numerical simulations. Similarly, the cases of N=3 and N=5 are also analyzed, with the obtained results shown in Supplementary Fig. 2a. It is found that Q still trends to infinite at $\alpha = 0$ for N=3 or N=5, and for the same $\alpha \neq 0$, the Q factor of quasi-BIC is larger for a larger N. In addition, the results also indicates that the Q factor is inversely proportional to the square of α (see Supplementary Fig. 2b). These results further confirm the existence of higher-order BICs.

Supplementary Note 2. Analytical derivation of *Q* factor of quasi-BIC resonances

To calculate the Q factor in Fig. 3, we define it as $Q = n_{\max} / \Delta n$ ($n = \sqrt{\varepsilon_d}$), where $n_{\max}$ is the refractive index corresponding to transmission peak and Δn is the full width half maximum bandwidth (FWHM). The relative permittivity of all cylinders are the same, i.e. ε_d, and the wave vector in cylinders is k_d. According to Eq. (1) and Eq. (2) in the main text, the transmission coefficient

$$T = \frac{1}{1 - i\sum_{i=1}^{N} X_i}, \tag{S1}$$

with

$$X_i = -\frac{\pi}{w}\sum_{i=1}^{N} \frac{R_i J_1(k_d R_i)}{\sqrt{\varepsilon_d} J_0(k_d R_i)}. \tag{S2}$$

As mentioned in the main text and shown in Supplementary Fig. 7, if all cylinders have different radii (i.e., $i \neq j, \alpha_i \neq \alpha_j$), N cylinders will lead to N-1 EIT windows and N-1 different Q factors. It is difficult to get the expression of each Q factor in a general case. Here in order to explore the relationship between N and Q factor, we consider a simple case: N-1 cylinders with radius R_a and only a cylinder with radius R_b. In this case, the system supports (N-2)-fold degenerate BICs, then only one EIT in transmission spectrum is left. Next, we will derive the Q factor of this EIT. In this case, Eq. (S2) can be written as

$$X = \frac{\pi}{w}\left[-(N-1)\frac{R_a J_1(k_d R_a)}{\sqrt{\varepsilon_d} J_0(k_d R_a)} - \frac{R_b J_1(k_d R_b)}{\sqrt{\varepsilon_d} J_0(k_d R_b)}\right]. \tag{S3}$$

Further, we set $x = \sqrt{\varepsilon_d}$ (refractive index), then $k_d R_{a(b)} = x k_0 R_{a(b)}$. Firstly, we find the permittivity of the transmission valleys, which corresponds to the solution of $J_0(s_v) = 0$. In this work, the considered parameters lead to s_2=5.52, which means $x_a = s_v / k_0 R_a$ and $x_b = s_v / k_0 R_b$. Because there are only two different sizes of all cylinders in the system, the asymmetry parameter is defined by $\alpha = (R_b - R_a)/R_a$. For $\alpha \in (0.99, 1.01)$, the value of $|x_a - x_b|$ is very small, then Taylor series of the Bessel functions around x_a and x_b are used:

$$\begin{aligned} J_0(x k_0 R_a) &\approx J_0(x_a k_0 R_a) - k_0 R_a J_1(x_a k_0 R_a)(x - x_a), \\ J_0(x k_0 R_b) &\approx J_0(x_b k_0 R_b) - k_0 R_b J_1(x_b k_0 R_b)(x - x_b). \end{aligned} \tag{S4}$$

Substituting Eq. (S4) to Eq. (S3) and using $J_1(x k_0 R_a) \approx J_1(x_a k_0 R_a)$, we get

$$X = \frac{\pi}{wk_0 x}\left(\frac{N-1}{x-x_a}+\frac{1}{x-x_b}\right). \tag{S5}$$

When $|T| = 1/2$, combining Eq. (S1) and (S5) leads to the following equation,

$$\left(\frac{N-1}{x-x_a}+\frac{1}{x-x_b}\right) = \pm\frac{\sqrt{3}wk_0 x}{\pi} . \tag{S6}$$

In Eq. (S6), the right-hand side of the equation is approximately equal to $\pm\sqrt{3}wk_0\left(x_a+x_b\right)/2\pi$. For easy analysis, we set

$$g_1 = \frac{\sqrt{3}wk_0}{\pi}\left(\frac{x_a+x_b}{2}\right),\ \ g_2 = -\frac{\sqrt{3}wk_0}{\pi}\left(\frac{x_a+x_b}{2}\right).$$

With g_1 and g_2, the solutions of Eq. (S6) are calculated as,

$$x_2^{(1)} = \frac{x_a+x_b}{2}+\frac{N}{2g_1}-\frac{\sqrt{g_1^{\,2}\left(x_a-x_b\right)^2+N^2+g_1\left(2N-4\right)\left(x_a-x_b\right)}}{2g_1} , \tag{S7a}$$

$$x_2^{(2)} = \frac{x_a+x_b}{2}+\frac{N}{2g_2}-\frac{\sqrt{g_2^{\,2}\left(x_a-x_b\right)^2+N^2+g_2\left(2N-4\right)\left(x_a-x_b\right)}}{2g_2} . \tag{S7b}$$

Because the value of $|x_a - x_b|$ is very small, $x_{\max}$ can take an approximation,

$$x_{\max} \approx \frac{x_a+x_b}{2}. \tag{S8}$$

Finally, the Q factor is defined by $Q = x_{\max}/\left|x_2^{(2)}-x_2^{(1)}\right|$, and after some simplifications, we have

$$Q = \frac{2N}{\left(x_a-x_b\right)^2}\frac{\pi}{\sqrt{3}wk_0} , \tag{S9}$$

where $x_a = s_v/\left(k_0R_a\right)$ and $x_b = s_v/\left(k_0R_b\right)$. Further, substituting x_a and x_b into the Eq. (S9) produces the following formula,

$$Q = \frac{2\pi k_0 R_b^{\,2}}{\sqrt{3}ws_v^2}\frac{N}{\alpha^2}. \tag{S10}$$

Using Eq. (S10), we can obtain the solid curve in the Fig. 4c in the main text.

Supplementary Note 3. Effective permittivity and permeability of waveguide junction.

The permittivity is modeled with waveguide dispersion of TE_{10} [1],

$$\varepsilon_{eff} = \varepsilon_b - \lambda^2 / 4H^2 , \tag{S11}$$

where ε_b is the relative permittivity of the medium filling the waveguide, H is height of waveguide, and λ is the working wavelength in free space. Eq. (S11) is similar to the Drude model. The red curve in Supplementary Fig. 8 shows the relationship between ε_{eff} and frequency. ε_{eff} changes slowly with frequency so that the ENZ window is a broadband. After doping a silicon rod into the waveguide junction, the effective permeability of the waveguide junction can be written as [2],

$$\mu_{eff} = 1 + \frac{A_0}{A}\left[\frac{2}{k_{Si}^{eff} R_0}\frac{J_1\left(k_{Si}^{eff} R_0\right)}{J_0\left(k_{Si}^{eff} R_0\right)} - 1\right], \tag{S12}$$

where $A_0 = \pi R_0^2$ is cross-sectional area of silicon rod, $A = L^2 - 3\times 16 \times \pi r_w^2$ is the total cross-sectional area of air region, r_w is the radius of metallic wires, $k_{Si}^{eff} = \sqrt{\varepsilon_{Si}^{eff}}\,\omega / c$ is the wave vector in silicon, and $\varepsilon_{Si}^{eff} = \varepsilon_{Si} - \lambda^2 / 4H^2$ is the effective permittivity of silicon for TE_{10} mode. Using Eq. (S12), we can obtain the relationship between μ_{eff} and frequency, as shown in Supplementary Fig. 8. As showed by the blue curve, μ_{eff} changes quickly with frequency, leading to the ZIM window that has an extremely narrowband response. One may broaden ZIM window by changing the material and shape of the dopant.

Supplementary Note 4. Geometry symmetry-free BIC induced by ENZ medium.

In ENZ medium, Eq. (1) in the main text can be generalized to [3],

$$T=\frac{1}{1-\left[ik_0\mu_1\left(S-S_d\right)/2w+\left(i\omega/2wH_1\right)\sum_{i=1}^{N}\oint_{\partial C_i}\vec{A}_i\cdot d\vec{l}\right]}, \tag{S13}$$

where $S=l\times w$ and S_d is the sum of areas of embedded objects. Likewise, we consider two cylinder objects for illustration and comparison. Supplementary Fig. 9a shows the calculated transmission vs both ε_d and α, from which a BIC can be seen at about $\varepsilon_d=4.82$ and $\alpha=0$, as indicated by the dashed circle. Supplementary Fig. 9b shows the transmission for $\alpha=-0.01$ case, and for comparison, numerical simulations were carried out using COMSOL with the geometry parameters that are same to that in Fig. 2. The obtained simulated results of two different location distribution cases are shown by the color balls. Both theoretical results and simulation results agrees well with each other. Similar EIT-like behavior is seen regardless of the locations of the two dielectric rods, and the total transmission indicated by the P corresponds to the quasi-BIC. The two valleys stem from monopole mode resonances that occur in either the left object (see the left pattern in Fig. 9c or d) or the right object one (see the right pattern in Fig. 9c or d). For the quasi-BIC, due to the term of $\tau=ik_0\mu_1\left(S-S_d\right)/2w$, the magnetic flux induced by two object are not exactly out of phase at all ((see the middle pattern in Fig. 9c or d)); the ENZ leads a modified condition: $\tau+\sum\Phi_i=0$ and $\prod\Phi_i<0$ for quasi-BIC. Note that the total transmission at about $\varepsilon_d=5.0$ is not BIC mode, which results from in phase resonances of EM wave inside two objects, corresponding the condition: $\tau+\sum\Phi_i=0$ and $\prod\Phi_i>0$. As $\alpha\to 0$, the induced flux Φ_i becomes very large, so $\left|\Phi_i\right|\gg\tau$. When $\alpha=0$, the term of $\tau=ik_0\mu_1\left(S-S_d\right)/2w$ can be negligible compared with Φ_i, so that the ideal BIC happens at $\sum\Phi_i=0$ and $\Phi_i\neq 0$, which coincides to the results revealed in the main text that the BIC mode is physically related to the nontrivial zeros of total magnetic flux in all embedded objects.

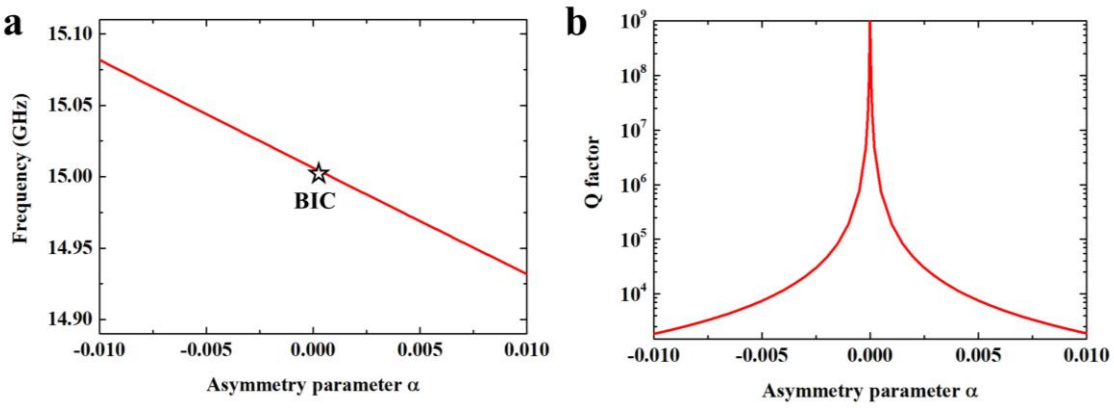

Supplementary Figure 1. Eigenfrequency of studied system for case of *N*=2. **a** Eigenfrequency as a function of asymmetry parameter. The eigenfrequency is about 15 GHz for $\alpha \in (-0.01, 0.01)$. The eigenmode turns to BIC mode at $\alpha = 0$. **b** *Q* factor vs asymmetry parameter $\alpha = 0$. The *Q* factor is infinite at $\alpha = 0$. Here in analysis, the related parameters are $R_1 = 8\,mm$, $\alpha = (R_2 - R_1)/R_1$, $\varepsilon_d = 4.82$ and $w = 44\,mm$.

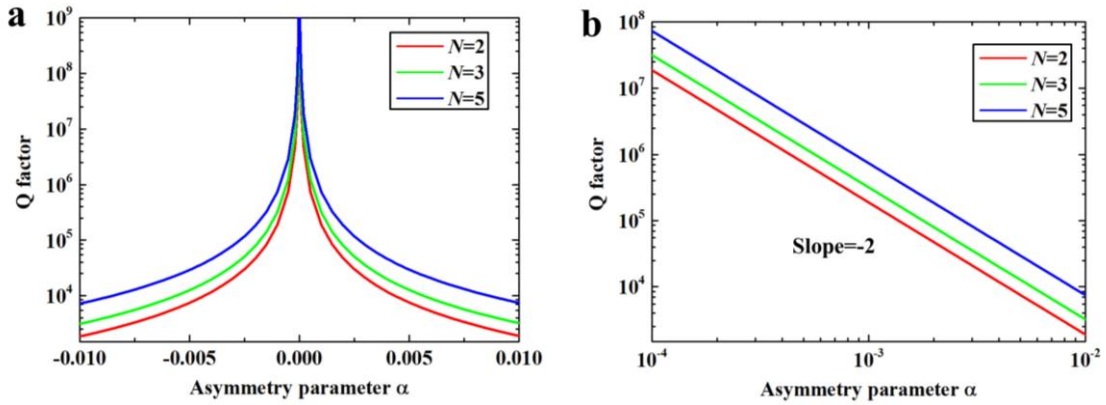

Supplementary Figure 2. The Q factor for the case of N objects that include (N-1) identical objects with a fixed radius of R_a, and one object with a variable radius of R_b. **a** Q factor of quasi-BICs vs asymmetry parameter $\alpha = 0$ for N=2 (red), N=3 (green) and N=5 (blue). Related parameters are $R_a = 8\,mm$, $\alpha = \left(R_b - R_a\right)/R_a$, $\varepsilon_d = 4.82$ and $w = 44\,mm$. **b** Log scale of **a**. N-dependent Q factor of linear shape can be observed. The vary trend of Q factor is consistent with Fig. 4c in the main text.

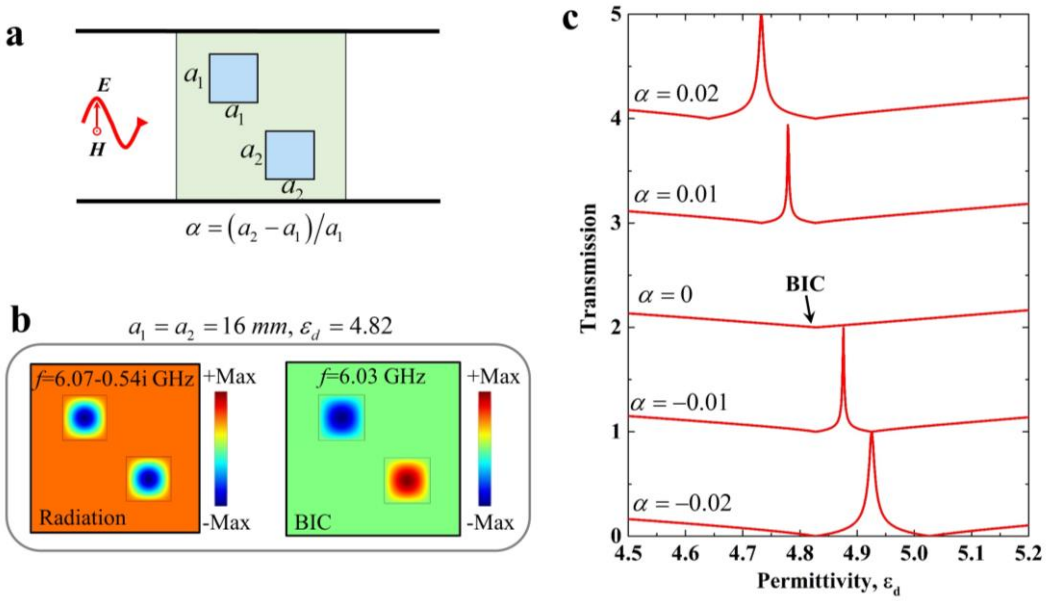

Supplementary Figure 3. Two square shape case. **a** A two-dimensional (2D) waveguide structure with two square dielectric embedded in ZIM. The side lengths of the two squares are a_1 and a_2, respectively. The asymmetry parameter is defined as $\alpha = (a_2 - a_1)/a_1$. **b** Eigenmode analysis with $a_1 = a_2 = 16\ mm$ and $\varepsilon_d = 4.82$. A symmetry mode and an antisymmetric mode were found around the frequency of 6.05 GHz. **c** Transmission vs ε_d for different α. For $\alpha \to 0$, the transmission peak becomes sharper. In the case of $\alpha = 0$, the EIT window is invisible in transmission spectrum. This is typical signature of a BIC mode manifested by a resonance with zero linewidth. In the simulation of transmission, we fix $a_1 = 16\ mm$ and the working frequency is 6.05 GHz.

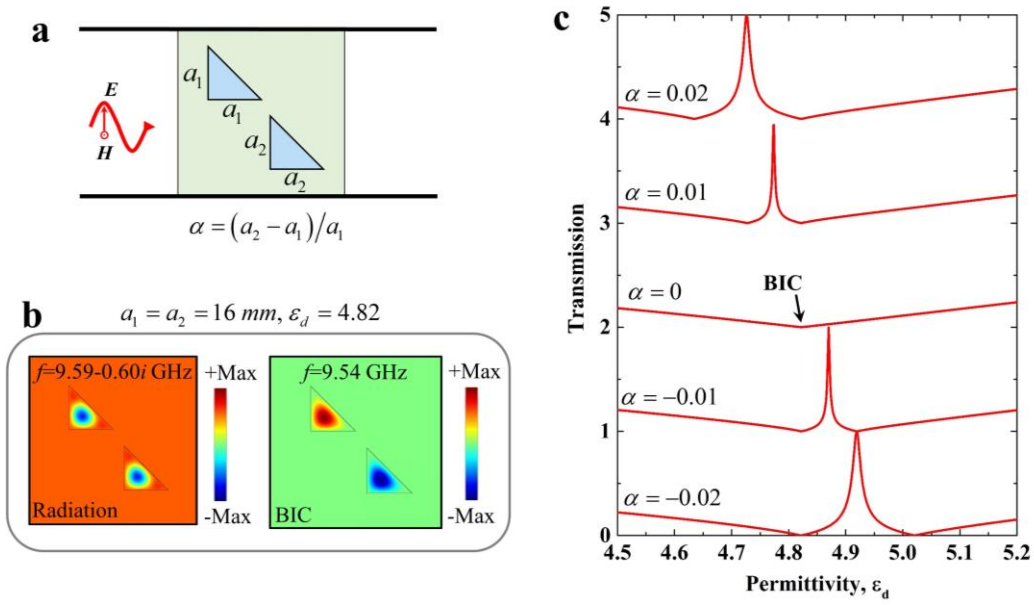

Supplementary Figure 4. Two isosceles-right triangular shape case. a A two-dimensional (2D) waveguide structure with two isosceles-right triangular embedded in ZIM. The right angle sides of triangles are a_1 and a_2, respectively. The asymmetry parameter is defined as $\alpha = (a_2 - a_1)/a_1$. **b** Eigenmode analysis with $a_1 = a_2 = 16\,mm$ and $\varepsilon_d = 4.82$. A symmetry mode and an antisymmetric mode were found around the frequency of 9.56 GHz. **c** Transmission *vs* ε_d for different α. In the simulation of transmission, we fix $a_1 = 16\,mm$ and the working frequency is 9.56 GHz.

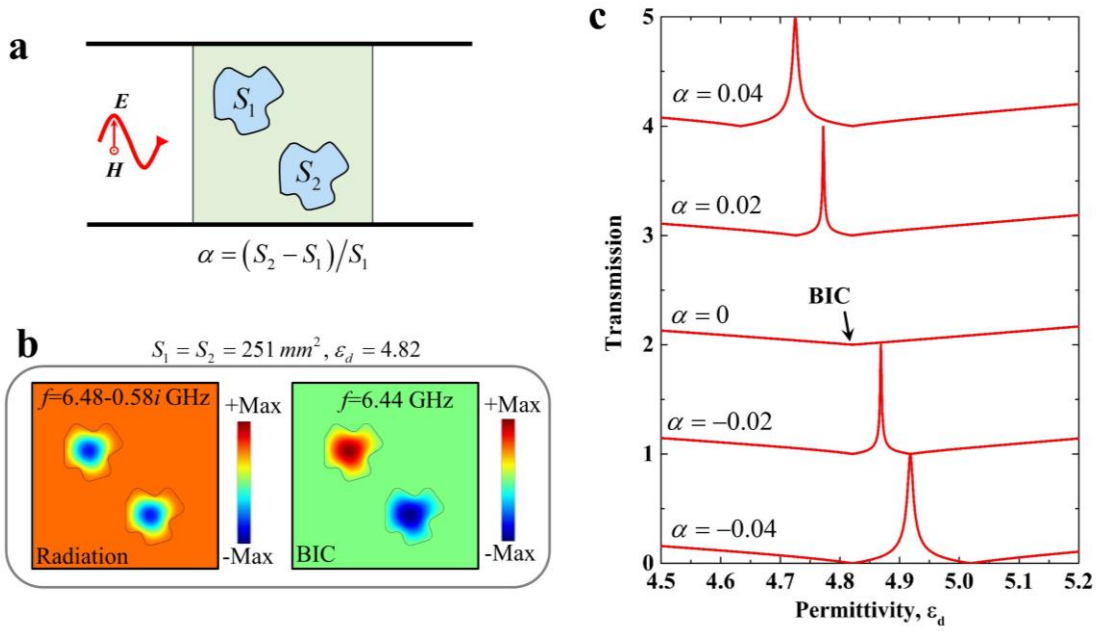

Supplementary Figure 5. Arbitrary shape case. a Two similar dielectric of arbitrary shape embedded in ZIM. The areas of dielectric are S_1 and S_2, respectively. The asymmetry parameter is defined as $\alpha = (S_2 - S_1)/S_1$. **b** Eigenmode analysis with $S_1 = S_2 = 251\,mm^2$ and $\varepsilon_d = 4.82$. A symmetry mode and an antisymmetric mode were found around the frequency of 6.46 GHz. **c** Transmission vs ε_d for different α. In the simulation of transmission, we fix $S_1 = 251\,mm^2$ and the working frequency is 6.46 GHz.

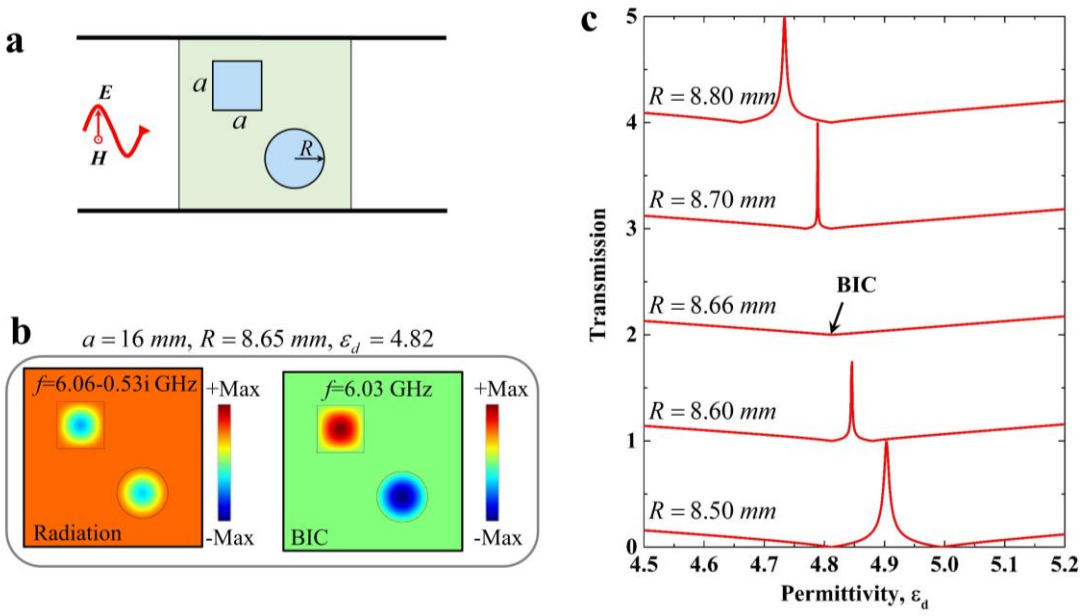

Supplementary Figure 6. The case of a square shape and a circular shape. a A square and a circular dielectric embedded in ZIM. The side length of the square is *a* and the radius of circle is *R*. **b** Eigenmode analysis with *a*=16 mm, *R*=8.65 mm, and $\varepsilon_d = 4.82$. There is no symmetry between the two objects but we still find a symmetry mode and an antisymmetric mode (BIC) around the frequency of 6.04 GHz. **c** Transmission changes as ε_d. In the simulation of transmission, we fix *a*=16 mm and the working frequency is 6.04 GHz. A zero line width of transmission is found at *R*=8.66 mm and $\varepsilon_d = 4.82$, which means a BIC here.

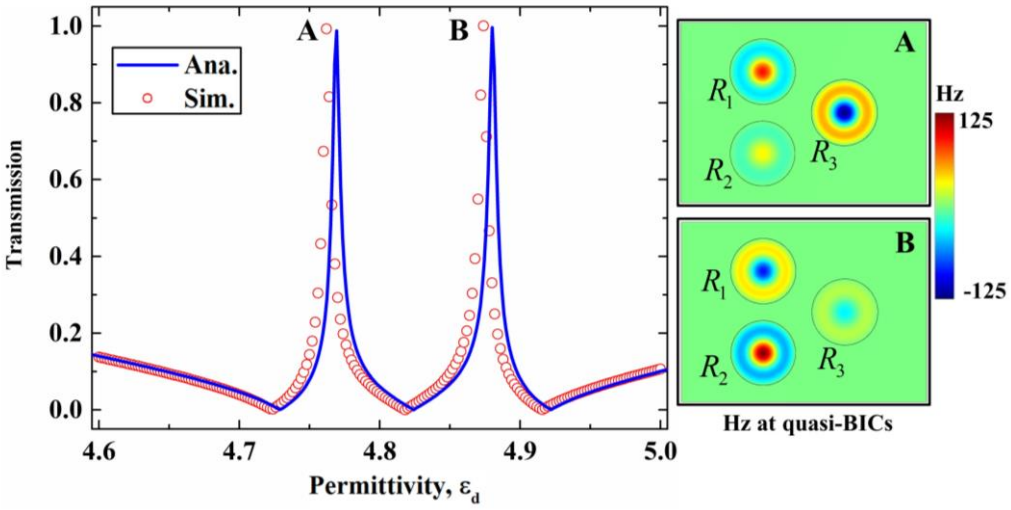

Supplementary Figure 7. Transmission spectrum for the case of *N*=3. The blue solid curve and red circles represent analytical and simulated results, respectively. Right panels are simulated out-of-plane magnetic field distribution at transmission peak A and peak B, respectively. In calculations, the working frequency is 15 GHz, $R_1 = 8\,mm$, $R_2 = 7.92\,mm$ and $R_3 = 8.08\,mm$, which means $\alpha_2 = (R_2 - R_1)/R_1 = -0.01$ and $\alpha_3 = (R_3 - R_1)/R_1 = 0.01$.

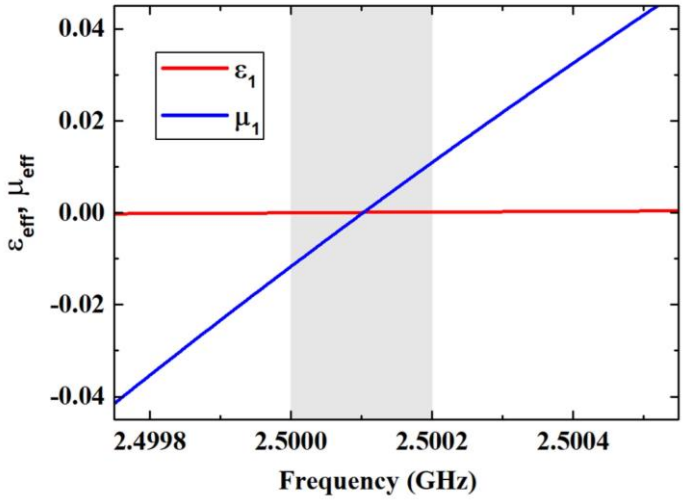

Supplementary Figure 8. Analytical prediction of the dispersion of effective permittivity and permeability of waveguide junction. The red curve and blue curve represent ε_{eff} and μ_{eff}. Although ε_{eff} changes slowly with frequency, μ_{eff} changes quickly with frequency lead to an extremely narrow ZIM window. Considering the problem of accuracy in simulation, we set R_0=14.0848 *mm* in theoretical calculations.

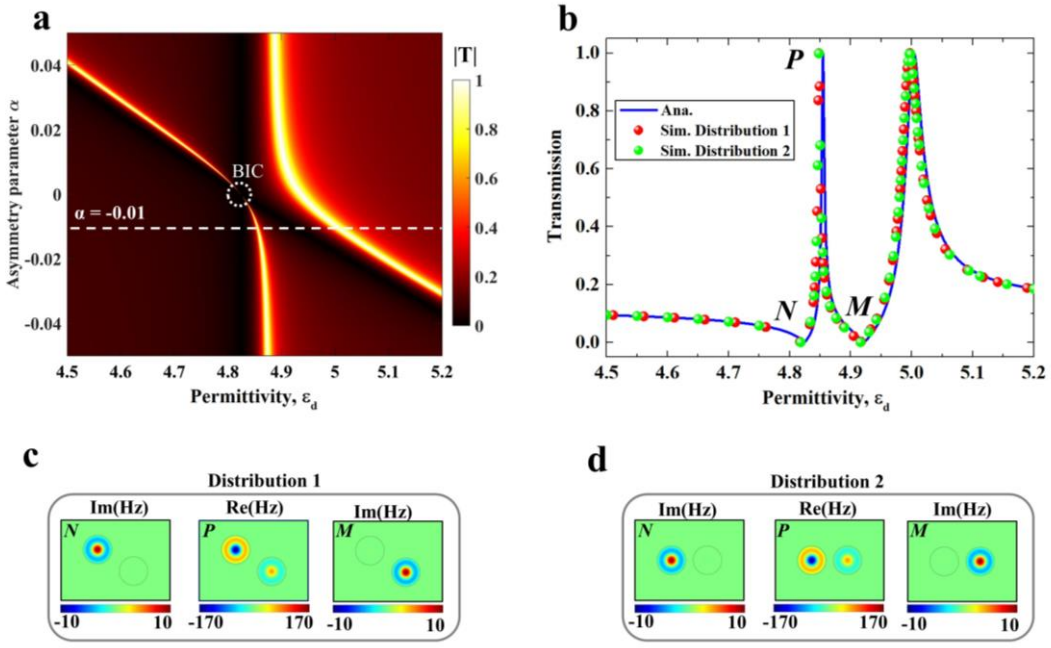

Supplementary Figure 9. BIC illustrations in ENZ-based host. a Analytical 2D map of transmission as a function of ε_d and asymmetry parameter α. The relevant parameters are as follows: R_1=8 mm, w = 44 mm, l = 60 mm and the working frequency is 15 GHz. **b** Transmission spectrum for $\alpha = -0.01$. The blue solid curve represents the analytical results. The red balls and green balls represent the simulated results for the two different distributions. Simulated magnetic field distribution patterns of distribution 1 and distribution 2 are shown in **c** and **d**, respectively. *M*, *N* and *P* corresponding to two transmission valleys and the peak, respectively. In simulations, the incident magnetic field is 1 A/m and ENZ is set as $\varepsilon_1 = 10^{-4}$ and $\mu_1 = 1$.

Supplementary References

1. Della Giovampaola, C. & Engheta, N. Plasmonics without negative dielectrics. *Phys. Rev. B* **93,** 195152 (2016).
2. Liberal, I., Mahmoud, A. M., Li, Y., Edwards, B. & Engheta, N. Photonic doping of epsilon-near-zero media. *Science* **355,** 1058-1062 (2017).
3. Xu, Y. & Chen, H. Total reflection and transmission by epsilon-near-zero metamaterials with defects. *Appl. Phys. Lett.* **98,** 113501 (2011).